Structural, Mössbauer and magnetic study of Co1-xZnxFe2O4 (x = 0.0 – 0.56) nano ferrites

S N Kane, R. Verma, S S Modak, V R Reddy, Frédéric Mazaleyrat

Structural, Mössbauer and magnetic study of $Co_{1-x}Zn_xFe_2O_4$ (x= 0.0–0.56) nano ferrites

S. N. Kane[1,*], R. Verma[1], S. S. Modak[2], V. R. Reddy[3], and F. Mazaleyrat[4]

[1] Magnetic materials laboratory, School of Physics, D. A. University, Khandwa Road, Indore – 452001, India

[2]Physics Department, Jaypee University of Engineering and Technology, Raghogarh, Guna 473226, India

[3] UGC-DAE Consortium for Scientific Research, Khandwa Road, Indore 452001, India

[4] SATIE, ENS Paris-Saclay, 4 Avenue des Sciences, 91190 Gif-sur-Yvette, France

Abstract:

We report on the synthesis of spinel $Co_{1-x}Zn_xFe_2O_4$ (x=0.0–0.56) ferrites by sol-gel auto-combustion method. X-ray diffraction 'XRD', magnetic measurements were used to study compositional–dependence of structural, magnetic properties, connection among them. Mössbauer spectroscopy was used to identify non-magnetic-phase, its effect on magnetic properties. Single-phased nano spinel-ferrite formation is confirmed by XRD. Increasing Zn-content leads to structural modifications such as decrease of lattice parameter, grain diameter D_{W-H}, alteration of inversion parameter, disorder, tensile-strain, dislocation density, variation of A–O–B, A–O–A, B–O–B super-exchange-interaction and canting angles. Cationic distribution suggests that Fe^{3+}, Co^{2+} ions reside on both A, B-sites, and with increasing Zn-content, B-site population of Fe^{3+}, Zn^{2+} ions increases; while that of Co^{2+} ions decreases. Saturation magnetization shows noticeable dependence on canting angle suggests that the magnetization in the studied samples is described by Yafet-Kittel three-sub-lattice model. Coercivity H_c values are consistent with anisotropy, and its dependence on D_{W-H} suggests that the studied samples are in overlap-region between multiple-domains/single-domain. Reduced-remanence indicate the variation of inter-grain magnetostatic-interaction, isotropic-behavior of multi-domain particles. Observed broad peaks in magnetization derivative with field suggest large-number of dislocations, more-uniform particle-size. Switching-field-distribution proposes potential application of the studied x=0.0 sample in high density recording, and sample with x=0.56 in targeted drug delivery. Mössbauer measurements confirm three-magnetic-components corresponding to A,B-sites, Fe3+ ions in grain boundaries/surface, Fe has 3+ oxidation state, and growing paramagnetic–doublet, alone does not explain the trend of M_s, suggesting that it is a collective-effect of structural-modification, presence of paramagnetic-doublet.

Key words: Mössbauer spectroscopy; XRD; magnetic measurements, SFD.

---

* Corresponding author: S. N. Kane, e mail: kane_sn@yahoo.com

1. Introduction

Ferrimagnetic spinel nano ferrites exhibit face centered cubic structure with two inter-penetrating sub-lattices tetrahedral A, octahedral B respectively allocated by divalent, trivalent metal ions, and are represented by formula $M^{2+}Fe^{3+}{}_2O_4$ [1]. Ferrite composition, synthesis technique, thermal treatment, grain diameter, cationic distribution, etc. can be effectively used for tuning their magnetic properties [2 – 9], making them useful for various applications e. g. - high density recording, targeted drug delivery applications, in high frequency applications, gas sensing, magnetic resonance imaging MRI. Use of x-ray diffraction XRD combined with magnetic measurements helps in understanding the magnetic properties, and their structural dependence. In spinel ferrites, Mössbauer spectroscopy is known to identify the presence of magnetic / non-magnetic phases e. g. in [10-12], to better understand the effect of various magnetic, non-magnetic phases on magnetic properties [9, 12,]. Co-ferrite has inverse spinel structure, while Zn-ferrite has normal spinel structure, so Co-Zn ferrite would show a mixed spinel structure. Accordingly, a controlled Zn-substitution in Co-ferrite will lead to a systematic modification of the distribution of cations on A, B site, and there would be a transformation from an inverse spinel to a mixed spinel, which in-turn will have visible effect on magnetic properties. Magnetic properties of nano Co-based ferrite differ from their bulk counterparts due to size dependence [13]. In nanoparticles, the large surface-to-volume ratio leads to dissimilar distribution of cations on A, B site as compared to their bulk counterparts [13-17]. So it is interesting to study the effect of composition, grain diameter, cationic distribution and presence of non-magnetic phase on structural, magnetic properties of Co-based ferrites. Literature [8, 13, 18 - 23] reports various studies on structural, and magnetic properties of spinel $Co_{1-x}Zn_xFe_2O_4$ ferrites, and focuses mainly on cation distribution dependence of magnetic properties, but the influence of non-magnetic component on magnetic properties is less-explored.

So in the present work we report sol gel auto-combustion synthesis of $Co_{1-x}Zn_xFe_2O_4$ (x = 0.0 – 0.56) ferrites, using nitrate-citrate precursors. XRD, magnetic measurements were used to study structural, magnetic properties, and correlation between them. ^{57}Fe Mössbauer spectroscopy was particularly used to detect the presence of non-magnetic phase, and its effect on magnetic properties.

2. Experimental details

Spinel ferrites with composition: $Co_{1-x}Zn_xFe_2O_4$ (x = 0.0 – 0.56) were synthesized by sol gel auto-combustion method, as explained in [6] utilizing 'AR' grade citrate-nitrate-acetate precursors: Ferric nitrate: $Fe(NO_3)_3.9H_2O$, Zinc nitrate: $Zn(NO_3)_2.6H_2O$, and Cobalt acetate: $Co(CH_3COO)_2.4H_2O$. Prepared 'dry gel' samples were used for room temperature XRD, Mössbauer, magnetic measurements.

Bruker D8 Advance diffractometer, utilizing CuK_α radiation (wavelength: 0.15406 nm) was used to get XRD data at room temperature. Room temperature transmission ^{57}Fe Mössbauer spectra were recorded in constant acceleration more using ^{57}Co:Rh source by using standard PC-based Mössbauer spectrometer equipped with Wissel velocity drive. Velocity calibration of the spectrometer is done with natural iron absorber at room

temperature. Room temperature hysteresis loops were obtained by Lakeshore Model 7410 vibrating sample magnetometer.

Cationic distribution was estimated by XRD peak intensities employing Bertaut method [24]. It gives cationic distribution by matching the computed, experimental intensity ratios for (422), (400), (220) planes as described in [25]. For dissimilar cation distribution on A, B sites the intensity ratio: $I_{(220)}/I_{(440)}$, $I_{(400)}/I_{(422)}$, $I_{(220)}/I_{(400)}$ varies. The best cation distribution amongst the site A, B for which theoretical, experimental ratios $I_{hkl}^{Obs.}$ and I_{hkl}^{Calc} of the observed, and calculated intensities agree noticeably, is taken to be the right one. Obtained cationic distribution was used to compute Néel magnetic moment '$\mathbf{n_N}$', theoretical magnetization at 0 K: $M_{s(th)}$, is calculated by using the formula: $n_N = M_B - M_A$ in Bohr magneton 'μ_B' where M_A, M_B are respectively magnetic moments of A, B-site obtained by cationic distribution. Conversion of $M_{s(th)}$ from μ_B to Am^2/kg is done using the following expression: $M_{s(th)} = [q \times \mu_B \times N_A] / m$, where, q - Neel magnetic moment, μ_B - 0.9274×10^{-20} emu, N_A – Avogadro's number, m - molecular weight ($g\ mol^{-1}$). Grain diameter $D_{W\text{-}H}$, strain ε, were obtained by Williamson-Hall plot. Dislocation density was computed by following expression:

$$\rho_D = 15\ \varepsilon / (a_{exp.} \times D_{W\text{-}H}) \quad (1)$$

Where ε – strain, $a_{exp.}$ – Experimental lattice parameter, $D_{W\text{-}H}$ – Grain diameter.

Specific surface area 'S' was obtained by following expression:

$$S = 6 / (\rho_{XRD} \times D_{W\text{-}H}) \quad (2)$$

Where ρ_{XRD} – X-ray density, $D_{W\text{-}H}$ – Grain diameter.

The interionic distances between cations – b, c, d, e, f , and between cation and anion – p, q, r, s were estimated the a_{exp} and $u^{\bar{4}3m}$ by using the following relations:

$$b = \frac{a_{exp.}\sqrt{2}}{4},\quad c = \frac{a_{exp.}\sqrt{11}}{8},\quad d = \frac{a_{exp.}\sqrt{3}}{4},\quad e = \frac{3a_{exp.}\sqrt{3}}{8},\quad f = \frac{a_{exp.}\sqrt{6}}{4} \quad (3)$$

$$p = a_{exp.} * \left(\frac{5}{8} - u^{\bar{4}3m}\right)$$
$$q = a_{exp.} * \sqrt{3} * \left(u^{\bar{4}3m} - \frac{1}{4}\right)$$
$$r = a_{exp.} * \sqrt{11} * \left(1 + u^{\bar{4}3m}\right)$$
$$s = a_{exp.} * \sqrt{3} * \left(\frac{u^{\bar{4}3m}}{3} + \frac{1}{8}\right) \quad (4)$$

Where, $a_{exp.}$ – Experimental lattice parameter, and $u^{\bar{4}3m}$ – Oxygen position parameter.

Theoretical lattice parameter $a_{th.}$, bond angles – θ_1, θ_2, θ_3, θ_4, θ_5, Oxygen position parameter – $u^{\bar{4}3m}$ were also computed by cationic distribution, utilizing the following equations:

$$a_{th} = \frac{8}{3\sqrt{3}}\left[(r_A + R_0) + \sqrt{3}(r_B + R_0)\right] \quad (5)$$

where, r_A – A-site ionic radius, r_B – B-site ionic radius, R_o – 0.138 nm is the radius of Oxygen ion.

$$u^{\bar{4}3m} = \frac{(r_A + R_o)}{(\sqrt{3} * a_{exp})} + \frac{1}{4} \quad (6)$$

where, R_o – 0.138 nm is the radius of Oxygen ion, a_{exp} – experimental lattice parameter.

$$\left.\begin{aligned} &\theta_1 = \cos^{-1}\left[\frac{p^2 + q^2 - c^2}{2pq}\right], \quad \theta_2 = \cos^{-1}\left[\frac{p^2 + r^2 - e^2}{2pr}\right], \quad \theta_3 = \cos^{-1}\left[\frac{2p^2 - b^2}{2p^2}\right] \\ &\theta_4 = \cos^{-1}\left[\frac{p^2 + s^2 - f^2}{2ps}\right], \quad \theta_5 = \cos^{-1}\left[\frac{r^2 + q^2 - d^2}{2rq}\right] \end{aligned}\right\} \quad (7)$$

where p, q, r, s – the distance between metal cations, and Oxygen anions (Me - O), b, c, d, e, f – the distance between metal−metal cations (M_e–M_e).

NORMOS program [26] was used to perform computer fitting of the Mössbauer spectra, with either overlapping of two sextets corresponding to tetrahedral A, B octahedral site, and a non-magnetic doublet or distribution of hyperfine fields. Saturation magnetization M_s, Coercivity H_c reduced remanence M_r/M_s were obtained from hysteresis measurements. Anisotropy constant K_1 was calculated by using the expression: $K_1 = (H_c \times M_s) / 0.96$, where M_s – saturation magnetization, H_c − coercivity. Hysteresis loops were also used to compute the magnetization derivatives dM / dH. Canting angle $\alpha_{Y\text{-}K}$ was computed as detailed in [8] using the equation : $\alpha_{Y\text{-}K} = \mathrm{Cos}^{-1}\{ (n^e_{B(x)} + M_{A(x)}) / M_{B(x)} \}$, where $M_{A(x)}$ and $M_{B(x)}$ are the magnetic moments expressed in Bohr magneton μ_B on A, B sites, and $n^e_{B(x)}$ is the experimental magnetic moment. Error bar shown in figures is standard deviation obtained from the data.

3. Results and discussions

XRD patterns of the studied samples are shown as fig.1 confirm the formation of single phase nanocrystalline spinel structure with grain diameter between 28.2 nm – 50.2 nm. Left inset of fig. 1 shows the expanded view of

311 peak, which shifts to higher two theta values, reveal that with increasing Zn-content lattice parameter $a_{exp.}$ increases. Perusal of right inset of fig. 1 depicts linear increase of $a_{exp.}$ predicted by Vegard's law [27], described by following experimental relation: $a_{exp.}$= 0.0025 (Zn content) + 0.8384.. Increase of $a_{exp.}$ is attributable to the fractional replacement of Co^{2+} ion whose ionic radius is 0.058 nm by Zn^{2+} ion whose ionic radius is 0.060 nm. In the studied samples the W-H plot with positive slope is indicative of the existence of tensile strain [28].

Fig. 2 (a) depicts the Zn-content dependence of D_{W-H}, described by following experimental relation: D_{W-H} = 50.5 – 40.9 (Zn-content). Fig. 2 a (inset) gives variation of dislocation density with D_{W-H} described by experimental relation: $\rho_D = 7.9 - 0.14 (D_{W-H})$. Decrease of D_{W-H} with Zn-content is attributable to: i) replacement of Co^{2+} ion with lower ionic radius by Zn^{2+} ion with higher ionic radius [29]; ii) increase of grain boundary curvature [30], associated with changes in lattice parameter.

Fig. 2 (b) depicts the variation of S with Zn-content, ascribable to increase of porosity [9], described by experimental relation: S = 31.6 (Zn-content) + 21.4. Fig. 2 b (inset) depicts variation of *S* with D_{W-H}, is attributed to well-known inverse relationship between S and D_{W-H} [7], described by experimental relation: S = 60.4 – 0.77 (D_{W-H}).

Fig. 2 (c) shows compositional dependence of tensile strain is attributable to composition-dependent variation of cationic distribution shown in table 1, depicts variation of Co^{2+}, Zn^{2+}, and Fe^{3+} ions population on A, B site [7], described by experimental relation: Strain = 0.0083 (Zn-content) + 0.0019. Fig. 2 (c) inset shows compositional dependence of ρ_D, and is attributed to compositional-dependent variation of cationic distribution shown in table 1, described by experimental relation: ρ_D = 5.89 (Zn-content) + 0.61.

Fig. 2 (d) depicts the variation of u with δ. Perusal of fig. 2 (d) shows linear decrease of u with δ, ascribable to the variation of disorder, as was also reported in [7, 31], described by linear relation: u = 0.385 – 0.006 (δ). In the studied samples, u varies between 0.3788 – 0.3807, which is higher than its ideal value of 0.375 [9], reveal enhanced disorder with respect to ideal spinel structure, and thus would mirror in magnetic properties [9]. As is known that Co-ferrite shows inverse spinel structure, and Zn-ferrite has normal spinel structure, so Zn-addition in Co-ferrite would lead to changes in the inversion degree δ. In the studied samples, with Zn-addition the δ varies between 0.67 – 1.0, shows that the spinel structure transforms from inverse-spinel to mixed-spinel. Inset of fig. 2 d shows dependence of D_{W-H} on inversion degree, is attributable to compositional dependence of cationic distribution shown in table 1 [7], and described by following experimental relation: $D_{W-H} = 62.2 (\delta) - 13.8$.

Computed cationic distribution is shown in table 1. Close agreement of: i) $a_{th.}$, $a_{exp.}$, and ii) Calc., Obs. intensity ratios - I_{220}/I_{440}, I_{400}/I_{422} , I_{220}/I_{440} , shown in table 1 confirms the reliability of the computed cationic distribution. Perusal of table 1 suggests that Fe^{3+}, Co^{2+} ions reside on both A, B sites, but Zn^{2+}, Co^{2+} ions are more populated on B-site than on A-site. With increasing Zn-content, the B-site population of Fe^{3+}, Zn^{2+} ions increases, and that of Co^{2+} ions decreases. Variation of cationic distribution leads to modification of inversion degree range between 0.67 – 1.0, Oxygen parameter range between 0.3786 – 0.3870 suggests the variation of disorder; and is consistent with earlier studies e. g. in - [6, 9].

Figure 3 shows the variation of bond angles with increasing Zn-content. Bond angles are closely related to the strength of A-O-B, B-O-B and, A-O-A super-exchange interaction [1]. Bond angles θ_1, θ_2 reveal information on A-O-B, θ_3 , θ_4 provide information on B-O-B and, θ_5 gives information on A-O-A super-exchange interaction [9, 32]. Perusal of fig. 3 shows that with increasing Zn-content, decrease of θ_1, θ_2, θ_5 suggests weakening of A-O-B, A-O-A interaction through concurrent increase of θ_3, θ_4 suggests strengthening of B–O–B interaction, and would reveal changes in magnetic properties is consistent with earlier studies e. g. in - [6, 9].

Hysteresis loops of the studied samples are depicted in fig. 4, while its inset shows linear decrease of $M_{s(exp.)}$ dependence with canting angle $\alpha_{y\text{-}k}$, described by fitting equation: $M_{s(exp.)} = 143.4 (\alpha_{y\text{-}k}) – 2.8$. Perusal of figure 4 inset shows that magnetization in the studied samples is described by Yafet-Kittel three sub-lattice model [10, 33], and the reduction of $M_{s(exp.)}$ is ascribable to of surface spin canting in spinel nano particles [20 – 21].

Fig. 5 (a) depicts the linear increase of H_c with K_1, and is consistent with earlier reports on Co-Zn ferrites e. g. – in [3, 9], described by experimental relation: $H_c = 58.6\ K_1 – 53.3$. Variation of H_c with $D_{W\text{-}H}$ as shown in the inset of fig. 5 a suggests that the studied ferrites lie in the overlap regions between multiple-domains/single-domain [3, 6, 9, 32]. Figure 5 (b) shows the Zn-content dependence of $M_{s(exp)}$, $M_{s(th)}$, and the non-similar trend of $M_{s(exp)}$, $M_{s(th)}$, shows that the magnetization behavior is governed by Yafet-Kittel three sub lattice model [10, 33]. In the studied samples M_r / M_s range between 0.206 – 0.423 indicate composition-dependent variation of inter-grain magneto static interaction, and isotropic behavior of multi-domain particles with no preferred direction of magnetization is consistent with literature [6, 9, 34-35].

Figure 6 a, c shows the hysteresis loops for samples with x = 0.16 and x = 0.56 while fig. 6 b, d shows the corresponding first derivative dM / dH. Perusal of fig. 6 b, d depicts the double-peak behavior, and reveal the competition between exchange coupling, and strong dipolar interactions [32, 36]. Broad dM / dH peaks reveal large number of dislocations in the crystalline samples, and is consistent with obtained dislocation density values [5], and is also associated to more stable structure of nanoparticle [37]. In the studied samples, with increasing Zn-content the peak height varies between 113 – 618, and increase of peak height indicates that the studied samples have a good magnetic state of crystalline cubic spinel structure [5, 38]. The full width at half maximum FWHM of first derivative varies between 676.99 – 3131.03 and lower FWHM values suggest that the particle size is more uniform [4]. Switching field distribution SFD is determined by using the expression: $SFD = \Delta H / H_c$, ΔH – full width at half maximum of the dM / dH. It is worth noting that the SFD has strong relation with the particle size distribution, and is also linked to distribution of particle coercivity [37- 39], because particles with different size, shape will tend to reverse at different magnetic field strengths. For the studied samples, SFD range between 2.6 – 24.7, and the observed SFD variation is ascribable to dissimilar particle size distribution [37]. Among the studied samples the sample with x = 0.0 shows lowest SFD - 2.6, and highest H_c - 1202.4 Oe would be most suitable for magnetic recording application [40], while sample with x = 0.56 shows lowest H_c -78.7 Oe, highest SFD - 24.7, would be more suitable for targeted drug delivery applications [4].

Figure 7 (a-f) depicts Mössbauer spectra, while the fitted hyperfine parameters, are shown in table 2. Mössbauer spectrum for x = 0.0 sample i.e., cobalt ferrite CFO shows magnetically split pattern characteristic of CFO phase with two sub-lattices. The two sextets correspond to A and B sites of the spinel ferrite. Following the literature, the sextet with higher internal field value is assigned to A-site, and the one with lower value is assigned to B-site [41]. The observed isomer shift shows that Fe has 3+ oxidation state for all the samples, is consistent with literature [9]. As the Zn content increases up to 0.08 an additional magnetic component with lesser hyperfine field is observed, this could be due to the presence of Fe^{3+} ions either in the grain boundaries or on the surface because of nano size effects [41]. In the studied samples, as the Zn-content increases higher than 0.08, the spectra are a combination of broad sextet, and a dominant paramagnetic doublet with quadruple splitting varying between 0.70 – 0.84 mm/s, and the doublet area range between 20 – 50 % which was not reported in earlier studies [8, 18] with similar compositions. The doublet is responsible for the observed changes in $M_{s(exp)}$, as seen in fig. 5 (b). Because of the broad features, the data is analyzed with distribution of hyperfine fields for samples with x > 0.08, and the computed hyperfine field distribution is shown in fig. 7 (g). The hyperfine field distribution shows three peaks at ~ 47, 40, and 27 Tesla in addition to the one at lower fields which could be due to the central paramagnetic component. Therefore, from the observed hyperfine field distribution features, one would conclude that three magnetic sextets corresponding to A-, B- sites of spinel phase and Fe^{3+} ions either in the grain boundaries or on the surface because of nano size effects. Further, as can be seen from table 2, the average hyperfine field, and the area fraction of magnetic sextet are found to decrease with Zn substitution roughly match with the trend of magnetization variation, expect for the x = 0.48 composition. Presence of a central paramagnetic−doublet alone does not explain the trend of saturation magnetization, leads to the conclusion that it is a combined effect of the alteration of structural parameters, and existence of paramagnetic-doublet. It is worth mentioning that, although the area fraction values of A, B site can give the distribution of Fe^{3+} ion on A, B site, but presence of the paramagnetic−doublet for samples with x higher than 0.08 makes it impossible to compute cationic distribution on each site, so cationic distribution could not be computed from Mössbauer spectra as was also reported in [9, 11].

4. Conclusions

XRD validates the formation of single phase nanocrystalline cubic spinel phase. Increase of lattice parameter is explained by partial replacement of Co^{2+} ion by Zn^{2+} ion. Alteration of cationic distribution leads to the variation of disorder, inversion degree, and A-B, B-B, A-B super-exchange interaction, which in-turn affects magnetic properties. Mössbauer spectra validate the presence of a paramagnetic-doublet, and confirm that Fe has 3+ oxidation state. Evolution of coercivity is consistent with corresponding anisotropy values. Dependence of coercivity on grain diameter shows that the studied samples lie in the overlap region of multiple/single domain region. Paramagnetic-doublet alone does not explain the trend of saturation magnetization, leads to the conclusion that it is a combined effect of the alteration of structural parameters, and existence of paramagnetic-doublet, and

thus facilitate better understanding of the compositional dependence of magnetic, non-magnetic phases, and their effect on magnetic properties. Magnetization derivative with field suggests uniform particle size, and presence of large-number of dislocations. Present studies display strong linking between structural, magnetic properties, and suggest potential applications of the studied samples in high density recording, and targeted drug delivery.

Acknowledgments: Authors thank Dr. M. Gupta UGC-DAE CSR, Indore, for XRD measurements. SNK acknowledges gratefully for one month "*Invited Professor*" stay at ENS Paris-Saclay, Cachan (France). This work is supported by Seed money grant: No. Dev/Seedmoney2.0/2020-21/649, 20 Jan. 2022 of Devi Ahilya University, Indore (India).

DECLARATIONS

Ethical Approval:

The authors declare that the ethical standards are maintained while writing this manuscript.

Consent to participate:

All authors voluntarily agree to participate in this study.

Consent for publication:

All the authors have read, agreed to give their consent for publication of the current version of the submitted manuscript.

Competing interests:

The authors declare that they have no known competing financial interests or personal relationships that could have appeared to influence the work reported in this paper.

Authors' contributions:

S. N. Kane: Conceptualization, Supervision, Resources, preparation of samples, sample characterization, data analysis, writing manuscript.

R. Verma: Structural data analysis, manuscript writing.

S. S. Modak: XRD data analysis, manuscript writing.

V. R. Reddy: Mössbauer characterization, data analysis, writing manuscript.

F. Mazaleyrat: Magnetic measurements, data analysis, manuscript writing.

Funding:

This work is supported by Seed money grant: No. Dev/Seedmoney2.0/2020-21/649, 20 Jan. 2022 of Devi Ahilya University, Indore (India).

Availability of data and materials:

The data sets generated during and/or analyzed during the current study are available from the corresponding author on reasonable request.

References

[1] Smit, J., Wijn, H.P.J.: Ferrites. Philips Technical Library, Eindhoven p.136 and 149 (1959)

[2] Mathew D. S., Juang R. S.: An overview of the structure and magnetism of spinel ferrite nanoparticles and their synthesis in microemulsions. Chemical Engineering Journal **129**, 51–65 (2007)

[3] Tiwari, P., Kane, S.N., Deshpande, U.P., Tatarchuk, T., Mazaleyrat, F., Rachiy, B.: Cr content dependent modification of structural, magnetic properties and bandgap in green synthesized Co–Cr nano-ferrites. Mol. Cryst. Liq. Cryst. **699**, 39–50 (2020)

[4] Shiv Kumar S., Singh R.R., Barman P. B.: Reitveld Refinement and Derivative Spectroscopy of Nanoparticles of Soft Ferrites (MgNiFe), Journal of Inorganic and Organometallic Polymers and Materials, **31**, 528 – 541 (2021)

[5] Dippong, T., Levei, E. A., Deac, I. G., Emilia Neag, E., Cadar, O: Influence of Cu^{2+}, Ni^{2+}, and Zn^{2+} Ions Doping on the Structure, Morphology, and Magnetic Properties of Co-Ferrite Embedded in SiO_2 Matrix Obtained by an Innovative Sol-Gel Route, Nanomaterials **10**, 580-1 – 580-12 (2020)

[6] Parmar, C., Verma, R., Modak, S. S., Mazaleyrat, F., and Kane, S. N.: Si^{9+} Ion-Irradiation Induced Modification of Structural and Magnetic Properties of Zn-Nanoferrite, ECS J. of Solid State Science and Technology **11**, 053015-1 053015-9 (2022)

[7] Kane, S.N., Tiwari, P., Deepti, Verma, R., Deshpande, U.P., Mazaleyrat, F.: Study of structural, magnetic properties and bandgap of spinel $Co_{1-x}Fe_{2+x}O_4$ ferrite. Mater. Today Proc. **32**, 358–364 (2020)

[8] Barrera, G., Coisson, M., Celegato, F., Raghuvanshi, S., Mazaleyrat, F., Kane, S.N., Tiberto, P.: Cation distribution effect on static and dynamic magnetic properties of $Co_{1-x}Zn_xFe_2O_4$ ferrite powders, J. Magn. Magn. Mater. **456,** 372–380 (2018)

[9] Tiwari, P., Verma, R., Modak, S. S., Reddy, V. R., Mazaleyrat, F., Kane, S. N.: ^{57}Fe Mössbauer study of $CoCr_xFe_{2-x}O_4$ nano ferrite, Hyperfine Interactions 242, 51-1 – 51-15 (2021)

[10] Tiwari P., Verma, R, Modak S. S., Reddy V. R., Kane S. N.: In-field ^{57}Fe Mössbauer study of $Mg_xZn_{1-x}Fe_2O_4$ prepared by green synthesis method, Hyperfine Interactions **243**, 7-1 – 7-15 (2022)

[11] Da Silva, S.W., Nakagomi, F., Silva, M.S., Franco, A., Garg, V.K., Oliveira, A.C., Morais, P.C.: Effect of the Zn content in the structural and magnetic properties of $Zn_xMg_{1-x}Fe_2O_4$ mixed ferrites monitored by Raman and Mossbauer spectroscopies. J. Appl. Phys. **107**, 09B503-1-09B503-3 (2010)

[12] Mele N. G., Gamarra D. A., Zélis P. M., Sánchez F. H., PasquevichG. A.: Evaluation of Nanoparticle-size distribution with Mössbauer Effect spectroscopy, Hyperfine Interactions **243**, 18-1 – 18-13 (2022)

[13] Gonsalves L. R, Gawas S. G., MeenaS. S., Verenkar V. M. S.: Size variation and magnetic dilution effects on the structure and magnetic properties of cobalt zinc ferrite, J. Mater. Sci: Mater. Electron. 33, 20144–20161 (2022)

[14] Peddis D., Yaacoub N., Ferretti M., Martinelli A., Piccaluga G., Musinu A., Cannas C., Navarra G., Greneche J. M., Fiorani D.: Cationic distribution and spin canting in $CoFe_2O_4$ nanoparticles, J. Phys.: Condens. Matter **23**, 426004-1 – 426004-8 (2011)

[15] Coey J. M. D., Noncollinear spin arrangement in ultrafine ferrimagnetic crystallites, Phys. Rev. Lett. **27**, 1140-1142 (1971)

[16] Tronc E., Prene P., Jolivet J. P., Dormann J. L., Greneche J. M.: Spin canting in Fe_2O_3. Hyperfine Interact. **112**, 97–100 (1997)

[17] Chinnasamy C. N., Jeyadevan B., Shinoda K., Tohji K., Djayaprawira D. J., M. Takahashi M., Joseyphus R.J., Narayanasamy A.: Unusually high coercivity and critical single-domain size of nearly monodispersed $CoFe_2O_4$ nanoparticles, , Appl. Phys. Lett. **83**, 2862-2864 (2003)

[18] Veverka M., Jirák Z., Kaman O., Knízek K., Maryško M., Pollert E., Záveta K., Lancok A., Dlouhá M., Vratislav S.: Distribution of cations in nanosize and bulk Co–Zn ferrites, Nanotechnology. **22**, 345701-1 – 34570 -7 (2011)

[19] Sawatzky G. A., Van Der Woude F., Morrish A. H.: Cation distributions in octahedral and tetrahedral sites of the ferrimagnetic spinel $CoFe_2O_4$, J. Appl. Phys. **39**, 1204–1205 (1968)

[20] Arulmurugan R., Vaidyanathan G., Sendhilnathan S., Jeyadevan B., Co-Zn ferrite nanoparticles for ferrofluid preparation: Study on magnetic properties, Phys. B Condens. Matter. **363**, 225–231 (2005)

[21] Arulmurugan R., Jeyadevan B., Vaidyanathan G., Sendhilnathan S.:Effect of zinc substitution on Co-Zn and Mn-Zn ferrite nanoparticles prepared by coprecipitation, J. Magn. Magn. Mater**. 288,** 470–477 (2005)

[22] Veverka M., Veverka P., Jirak Z., Kaman O., Knızek K., Marysko M., Pollert E., Zaveta K.:Synthesis and magnetic properties of $Co_{1-x}Zn_xFe_2O_{4+\gamma}$ nanoparticles as materials for magnetic fluid hyperthermia, J. Magn. Magn. Mater. **322**, 2386-2389 (2010)

[23] Raghuvanshi S., Kane S. N., Tatarchuk T. R., Mazaleyrat F.: Effect of Zn Addition On Structural, Magnetic Properties, Antistructural Modeling Of $Co_{1-x}Zn_xFe_2O_4$ Nano ferrite, AIP Conf. Proc. **1953**, 030055-1 – 030055-4 (2018)

[24] Bertaut E. F., Etude de la nature des ferrites spinelles. Comptes Rendus Hebdomadaires des Seances de I'Academie des Sciences **230,** 213-215 (1950).

[25] Tanna, A. R., Joshi, H. H.: Computer Aided X-Ray Diffraction Intensity Analysis for Spinels: Hands-On Computing Experience, World Academy of Science, Engineering and Technology, International Journal of Physical and Mathematical Sciences **7 (3)**, 334–341 (2013).

[26] Brand, R.A.: Improving the validity of hyperfine field distributions from magnetic alloys: part I: Unpolarized source. Nucl. Instrum. Methods **B. 28**, 398–416 (1987)

[27] Denton, A. R., Ashcroft, N.W.: Vegard's law, Phys. Rev. **A 43,** 3161–3164 (1991)**.**

[28] Zak A. K., Majid W.H. A, Abrishami M.E., Yousefi R.: X-ray analysis of ZnO nanoparticles by Williamson-Hall and size–strain plot methods, Solid State Sciences **13**, 251–256 (2011)

[29] Hu J., Maa Y., Kan X., Liu C., Zhang X., Rao R., Wang M. Zheng G.: Investigations of Co substitution on the structural and magnetic properties of Ni-Zn spinel ferrite. Journal of Magnetism and Magnetic Materials **513**, 167200-1 - 167200-8 (2020)

[30] Vollath, D.: Nanoparticles – Nanocomposites –Nanomaterials An Introduction for Beginners, p. 30. Wiley-VCH Verlag, Weinheim (2013)

[31] Tiwari P., Kane S.N., Verma R., Tatarchuk T., Mazaleyrat F., (Chapter 29) Nanochemistry, Biotechnology, Nanomaterials, and Their Applications, Springer Proceedings in Physics, Springer International Publ. Co., part of Springer Nature 2019, Chapter 29, pp. 431–442, O. Fesenko, L. Yatsenko (eds.), Nanocomposites, Nanostructures, and Their Applications, Springer Proceedings in Physics 222

[32] Kolhatkar, A.G., Jamison, A.C., Litvinov, D., Willson, R.C., Randall Lee, T.: Tuning the Magnetic Properties of Nanoparticles. Int. J. Mol. Sci. **14**, 15977–16009 (2013)

[33] Satya Murthy, N.S., Natera, M.G., Youssef, S.I., Begum, R.J., Srivastava, C.M.: Yafet-Kittel Angles in Zinc-Nickel Ferrites. Phys. Rev. **181**, 969–977 (1969)

[34] Stoner E. C., Wohlfarth E. P.: A mechanism of magnetic hysteresis in heterogeneous alloys. Philosophical Transactions of the Royal Society of London **240**, 599–642(1948)

[35] Shirsath, S.E., Toksha, B.G., Jadhav, K.M.: Structural and magnetic properties of In3+ substituted $NiFe_2O_4$. Mater. Chem. Phys. **117**, 163–168 (2009)

[36] Ateia E. E., Ateia M. A., Arman M. M.: Assessing of channel structure and magnetic properties on heavy metal ions removal from water, J Mater Sci: Mater Electron **33**, 8958–8969 (2022).

[37] Kumar S., Barman P.B., Singh R. R.: Estimation and association of structural, elastic and magnetic properties of magnesium-nickel-ferrite nanoparticles annealed at different temperatures, Mater. Sci. Eng. **B 272**, 115362-1 - 115362-16 (2021)

[38] Muthuselvam I. P., Bhowmik R.N.: Mechanical alloyed Ho^{3+} doping in $CoFe_2O_4$ spinel ferrite and understanding of magnetic nanodomains. J. Magn. Magn. Mater. **322**, 767–776 (2010)

[39] Jiles D., *Introduction to Magnetism and Magnetic Materials* (Chapman and Hall, New York, 1991)

[40] Lodder J. C., Handbook of Magnetic Materials, chapter 2, Magnetic recording hard disk thin film media, in Handbook of Magnetic Materials, **11** 291-405 (1998). https://doi.org/10.1016/S1567-2719(98)11006-5

[41] Chinnasamy C. N., Narayanasamy A., Ponpandian N., Chattopadhyay K, Shinoda K, Jeyadevan B., Tohji K., Nakatsuka K., Furubayashi T., Nakatani I.: Mixed spinel structure in nanocrystalline $NiFe_2O_4$. Phys. Rev. **B 63**, 184108-1 – 184108-6 (2001)

Table 1: Cation distribution (for A, B site), experimental, theoretical lattice parameter (a_{exp}, a_{th}), for $Co_{1-x}Zn_xFe_2O_4$ ferrite as a function of Zn content (x), and calculated, observed values of intensity ratios I_{220}/I_{440}, I_{400}/I_{422} , I_{220}/I_{440}.

X	Cation distributions	a_{exp} (nm) (± 0.0007)	a_{Th} (nm) (± 0.0012)	I_{220}/I_{440}		I_{400}/I_{422}		I_{220}/I_{440}	
				Calc.	Obs.	Calc.	Obs.	Calc.	Obs.
0.0	$(Co^{2+}_{0.06}Fe^{3+}_{0.94})^{A}[Co^{2+}_{0.94}Fe^{3+}_{1.06}]^{B}$	0.8387	0.8375	0.858	0.911	2.5401	2.641	1.482	1.513
0.08	$(Co^{2+}_{0.00}Zn^{2+}_{0.00}Fe^{3+}_{1.00})^{A}[Co^{2+}_{0.92}Zn^{2+}_{0.08}Fe^{3+}_{1.00}]^{B}$	0.8379	0.8409	0.864	0.922	2.565	2.612	1.413	1.464
0.16	$(Co^{2+}_{0.00}Zn^{2+}_{0.05}Fe^{3+}_{0.95})^{A}[Co^{2+}_{0.84}Zn^{2+}_{0.11}Fe^{3+}_{1.05}]^{B}$	0.839	0.8406	0.978	1.013	2.192	2.079	1.485	1.513
0.32	$(Co^{2+}_{0.00}Zn^{2+}_{0.11}Fe^{3+}_{0.89})^{A}[Co^{2+}_{0.68}Zn^{2+}_{0.21}Fe^{3+}_{1.11}]^{B}$	0.8396	0.8404	0.9157	1.016	2.021	1.975	1.381	1.432
0.48	$(Co^{2+}_{0.19}Zn^{2+}_{0.10}Fe^{3+}_{0.71})^{A}[Co^{2+}_{0.33}Zn^{2+}_{0.38}Fe^{3+}_{1.29}]^{B}$	0.8393	0.8400	0.899	1.023	2.0203	1.931	1.5701	1.632
0.56	$(Co^{2+}_{0.29}Zn^{2+}_{0.04}Fe^{3+}_{0.67})^{A}[Co^{2+}_{0.15}Zn^{2+}_{0.52}Fe^{3+}_{1.33}]^{B}$	0.8398	0.8394	0.951	1.05	2.103	2.095	1.384	1.421

Table 2: Fitted Mössbauer parameters (Width – Line width, *I. S.- Isomer shift, relative to α-Fe, Q. S. – quadrupole splitting, B_{hf}– Hyperfine field*, *area - % Area of the sextet and/or* doublet) for the studied $Co_{1-x}Zn_xFe_2O_4$ ferrite samples as a function of Zn content.

Sample (x)	**Component (Site)**	**Width (mm/s) (±0.02)**	**I.S. (mm/s) (±0.1)**	**Q.S. (mm/s) (±0.02)**	**B_{HF} (Tesla) (±0.1)**	**Area (%) (±2)**
0.0	Sextet (A)	0.46	0.36±0.01	-0.04	51.6	32
	Sextet [B]	0.57	0.29±0.01	-0.01	48.6	68.
0.08	Sextet	0.54	0.29 ± 0.01	-0.02	47.6	32
	Sextet	0.56	0.31 ± 0.01	-0.01	50.1	23
	Sextet	1.22	0.45 ± 0.04	-0.19	42.0	25
	Doublet	0.97	0.31 ± 0.01	0.84	–	20
0.16	Sextet	0.4	–	–	<36.9>	65
	Doublet	0.64	0.34 ± 0.01	0.77	–	35
0.32	Sextet	0.4	–	–	<37.9>	76
	Doublet	0.65	0.32 ± 0.01	0.72	---	24
0.48	Sextet	0.4	–	–	<28.9>	61
	Doublet	0.67	0.30 ± 0.01	0.70	---	39
0.56	Sextet	0.4	–	–	<25.4>	50
	Doublet	0.69	0.31 ± 0.01	0.72	–	50

FIGURECAPTIONS:

FIGURE 1. XRD patterns of the studied $Co_{1-x}Zn_xFe_2O_4$ ferrites, Inset: (left panel) gives zoom part of 311 reflection showing peak shift, (right panel) compositional dependence of $a_{exp.}$.

FIGURE 2. Zn-content dependence of: (a) grain diameter (Inset: variation of dislocation density with grain diameter), (b) –S (Inset: variation of specific surface area with grain diameter), (c) strain (Inset: variation of dislocation density with Zn-content). (d) Variation of Oxygen parameter with degree of inversion (Inset: variation of grain diameter with degree of inversion). Continuous lines are linear fit to the data.

FIGURE 3. Zn-content dependence of bond angles ($\theta_1^{A\text{-}O\text{-}B}$, $\theta_2^{A\text{-}O\text{-}B}$, $\theta_3^{B\text{-}O\text{-}B}$, $\theta_4^{B\text{-}O\text{-}B}$, $\theta_5^{A\text{-}O\text{-}A}$).
Line connecting points are guide to the eye.

FIGURE 4. Hysteresis loops of the studied samples. Inset: variation of $M_{s\ (exp.)}$ with of $\alpha_{y\text{-}k}$.

FIGURE 5. (a) Variation of H_c with K_1, (Inset: Variation of H_c with $D_{W\text{-}H}$, line connecting points is guide to the eye),

(b) compositional dependence of $M_{s(exp.)}$, $M_{s(th.)}$ at 0 K (and corresponding Neel magnetic moment values in Bohr magneton 'μ_B' are also shown), line connecting points is guide to the eye.

FIGURE 6. (a) Representative hysteresis loops (a: for x = 0.16, c: x = 0.56), and corresponding first derivative
(b: x = 0.16, d: x = 0.56).

FIGURE 7. (a – f) Room temperature Mössbauer spectra of the studied samples. Symbols: experimental data, lines: best fit to the experimental data (Sextet: shown in red, blue color; Doublet: shown in gray color). (g) Hyperfine field distribution.

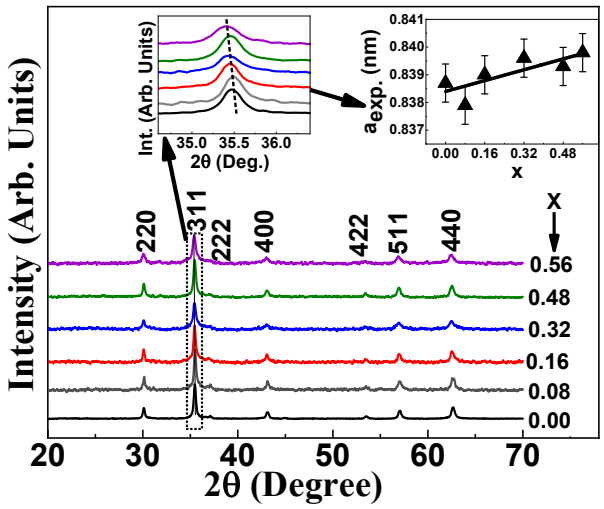
Intensity (Arb. Units)
2θ (Degree)
20
30
40
50
60
70
220
311
222
400
422
511
440
X
0.56
0.48
0.32
0.16
0.08
0.00
Int. (Arb. Units)
35.0
35.5
36.0
2θ (Deg.)
a_exp. (nm)
0.841
0.840
0.839
0.838
0.837
0.00
0.16
0.32
0.48
x

FIGURE 1

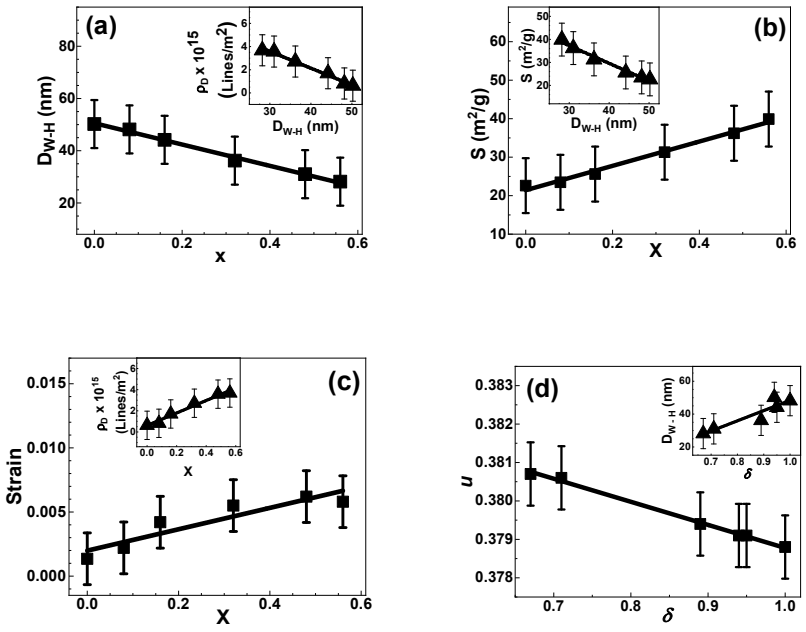
(a)
D_{W-H} (nm)
x
ρ_D x 10^{15} (Lines/m^2)
D_{W-H} (nm)
(b)
S (m^2/g)
X
S (m^2/g)
D_{W-H} (nm)
(c)
Strain
X
ρ_D x 10^{15} (Lines/m^2)
X
(d)
u
δ
D_{W-H} (nm)
δ

FIGURE 2

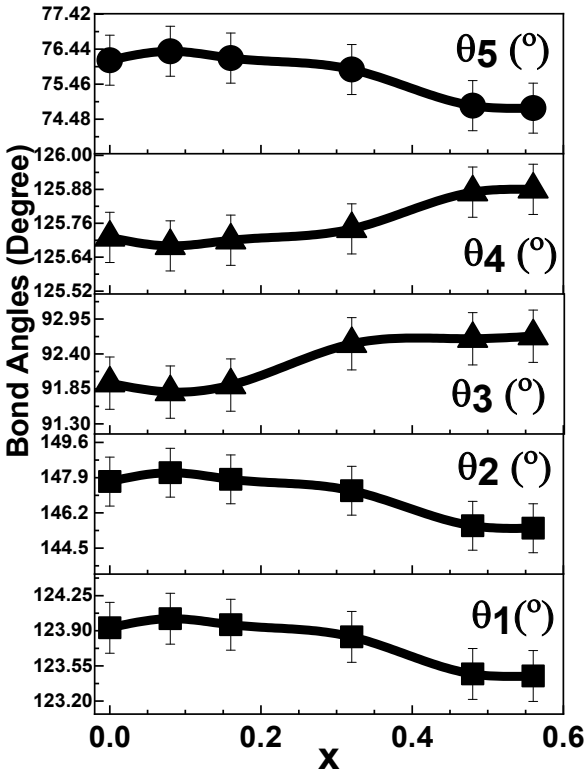
Bond Angles (Degree)
θ5 (°)
θ4 (°)
θ3 (°)
θ2 (°)
θ1(°)
77.42
76.44
75.46
74.48
126.00
125.88
125.76
125.64
125.52
92.95
92.40
91.85
91.30
149.6
147.9
146.2
144.5
124.25
123.90
123.55
123.20
0.0
0.2
0.4
0.6
x

FIGURE 3

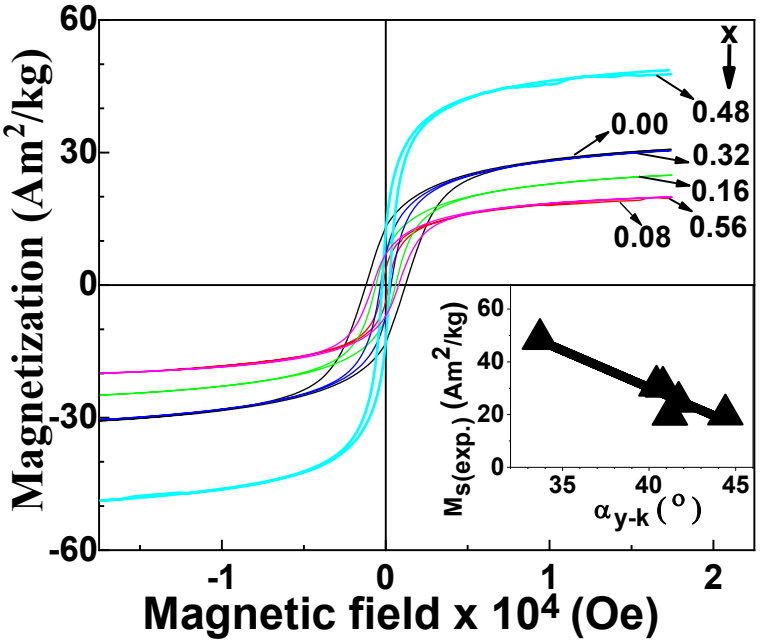
Magnetization (Am²/kg)
Magnetic field x 10⁴ (Oe)
60
30
0
-30
-60
-1
0
1
2
x
0.48
0.00
0.32
0.16
0.08
0.56
M_S(exp.) (Am²/kg)
60
40
20
0
35
40
45
α_y-k (°)

FIGURE 4

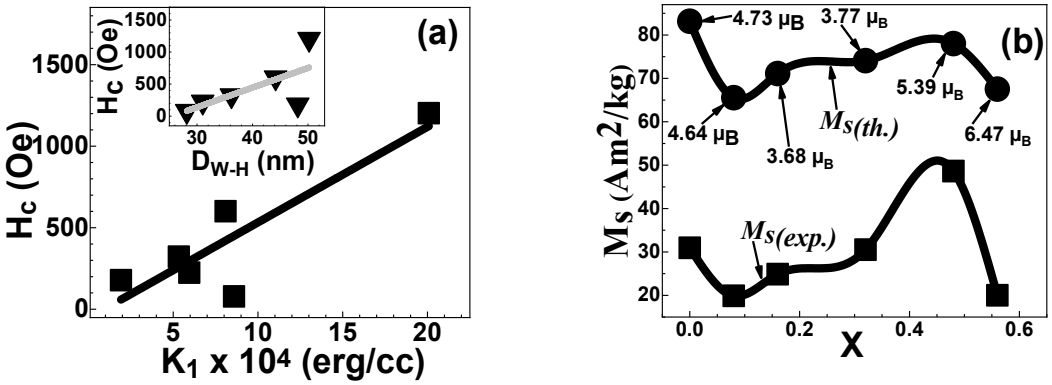
(a)
Hc (Oe)
K1 x 10⁴ (erg/cc)
DW-H (nm)
(b)
4.73 μB
3.77 μB
5.39 μB
4.64 μB
3.68 μB
6.47 μB
Ms(th.)
Ms(exp.)
MS (Am²/kg)
X

FIGURE 5

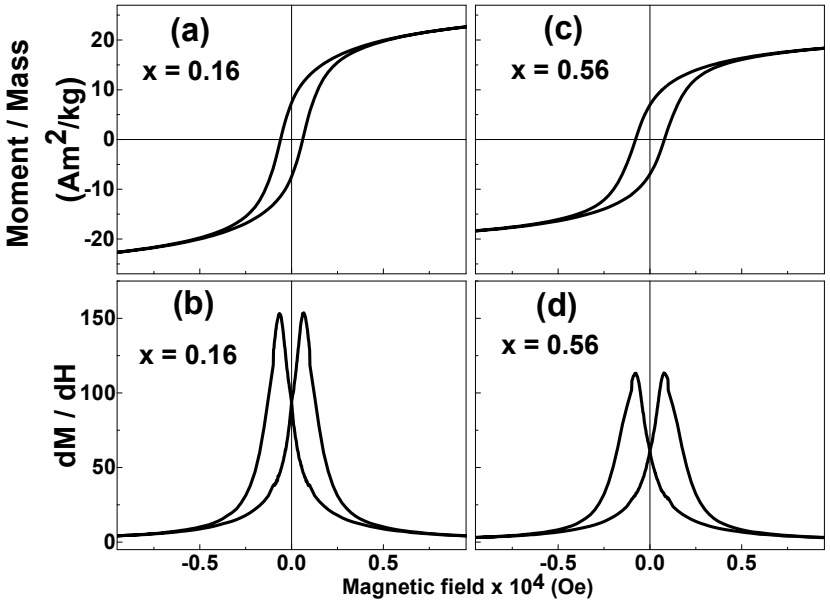
(a)
x = 0.16
(c)
x = 0.56
(b)
x = 0.16
(d)
x = 0.56
Moment / Mass
(Am2/kg)
dM / dH
Magnetic field x 10^4 (Oe)
20
10
0
-10
-20
150
100
50
0
-0.5
0.0
0.5

FIGURE 6

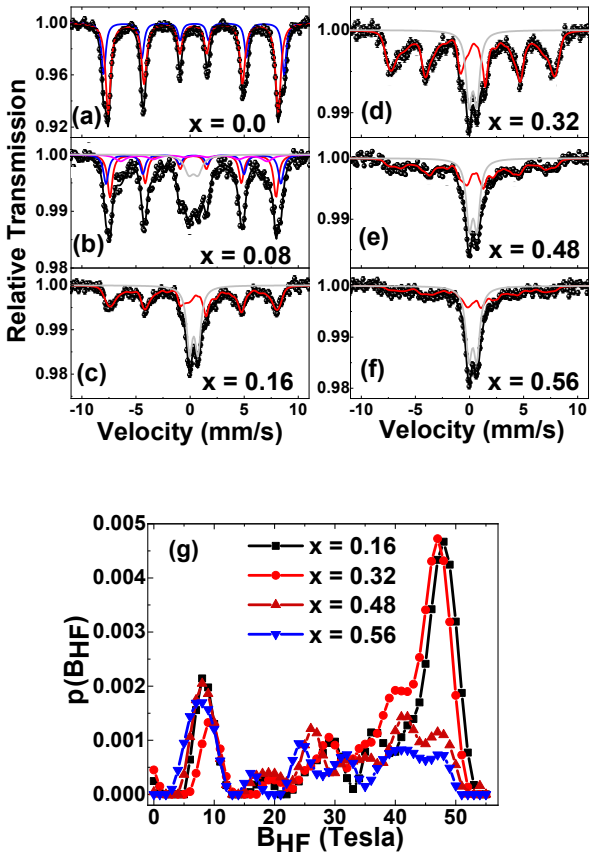
Relative Transmission
(a)
x = 0.0
(b)
x = 0.08
(c)
x = 0.16
(d)
x = 0.32
(e)
x = 0.48
(f)
x = 0.56
Velocity (mm/s)
Velocity (mm/s)
(g)
x = 0.16
x = 0.32
x = 0.48
x = 0.56
p(B_HF)
B_HF (Tesla)

FIGURE 7